Drivers and Mechanisms of the 2021 Pacific Northwest Heatwave

D. L. Schumacher[1], M. Hauser [1], and S. I. Seneviratne[1]

[1]Institute for Atmospheric and Climate Science, Department of Environmental Systems Science, ETH Zurich, Zurich, Switzerland

Corresponding author: Dominik L. Schumacher (dominik.schumacher@env.ethz.ch)

Key Points:

- A strong 'Omega Block' enabled the heatwave, yet near-surface air temperatures were more extreme than suggested by the large-scale flow
- The sinking and thus adiabatically heated air aloft previously experienced strong latent heating over the Pacific Ocean
- Deep atmospheric boundary layers, fueled by mountains and dry soils in the region, brought the unprecedented heat down to the surface

Abstract

In late June 2021, western North America, and in particular the Pacific Northwest experienced temperatures usually associated with hot desert climates. Using a blend of reanalysis data and Earth System Model (ESM) simulations, we disentangle the physical drivers underlying this exceptional event. A recent investigation has revealed the aggravating effect of human-induced climate change, while another study examined the dynamics behind the strong 'Omega Block'. Nevertheless, both drivers cannot fully explain how the extreme heat was reached. Our analysis highlights the role of the anticyclonic circulation aloft, which converted previously gained potential energy — some of which by intense latent heating thousands of kilometers upwind over the North Pacific — back into hot air through subsidence. We demonstrate that this upwind latent heat release not only resulted in a hot troposphere above the heatwave region, but also contributed directly to escalating near-surface temperatures. Facilitated by the mountainous terrain and dry soils in the region, deep atmospheric boundary layers were established over the course of several days, connecting the air close to Earth's surface to a massive heat reservoir many kilometers above. Overall, we consider this mega-heatwave the outcome of an intricate interplay between dynamic and thermodynamic processes. Nevertheless, our ESM experiments suggest that the same large-scale atmospheric circulation — fueled by thermodynamic drivers such as more available moisture for condensation upwind — could enable even more extreme near-surface temperatures. We identify regions prone to experience events with similar characteristics, and discuss the implications of our findings with increasing global warming.

Plain Language Summary

In late June 2021, western North America, and in particular the Pacific Northwest experienced temperatures normally encountered in hot deserts. Our analysis highlights the role of the anticyclonic circulation aloft, whose downward spiraling air masses converted previously gained potential energy back into heat. We show that on top of this heating through sinking, the air was previously heated by condensation in ascending air streams thousands of kilometers upwind, over the North Pacific. This upwind heat release resulted in hotter air above the heatwave region than already implied by the large-scale sinking motion, and contributed to escalating near-surface temperatures. Facilitated by mountainous terrain and dry soils in the region, strong vertical mixing connected the air close to Earth's surface to a massive heat reservoir many kilometers above. Overall, we consider this mega-heatwave the outcome of an intricate interplay of the atmospheric flow and processes such as condensational and surface heating, further exacerbated by human-induced background warming. Our experiments suggest that if fueled by more available moisture for condensation upwind, the same large-scale atmospheric circulation could enable even more extreme near-surface temperatures. Lastly, we identify regions prone to experience similar events and discuss the implications of our findings with increasing global warming.

1 Introduction

In the summer of 2021, a heatwave eclipsed existing temperature records in the Pacific Northwest (PNW). The extreme heat culminated in late June in the most densely populated coastal areas, where several hundred excess deaths were reported (BMJ, 2021). Epitomized by

temperatures of nearly 50°C at about 50°N (e.g., Samenow & Livingston, 2021), and considered to be one of the most extreme weather events on record (Thompson et al., 2022), the sheer intensity of this heatwave mandates a detailed understanding of its causes. From an atmospheric perspective, the temperature escalations were fostered by a strong 'Omega Block' in the region that slowly shifted eastwards. Atmospheric blockings are known to enable intense heatwaves in the midlatitudes, as their slowly subsiding — and hence warming — anticyclonic air masses shield the region underneath from storms and provide clear skies (Rex 1950; Xoplaki et al., 2003; Trigo et al., 2005; Sousa et al., 2017). A rapid attribution study suggests that an event of this magnitude has become at least 150 times more likely due to anthropogenic climate change, and that an event with the same occurrence of probability in a pre-industrial climate would have been 2°C less hot (Philip et al., in review). This analysis and other studies have provided strong evidence of human influence on both the occurrence and magnitude of extreme weather events (e.g., Stott et al., 2004; Otto et al., 2012; Russo et al., 2015; Trenberth et al., 2015; Stott et al., 2016; Hauser et al., 2016; Wehrli et al., 2019, in review; van Oldenborgh et al., 2021). Even in consideration of this human-induced aggravation, it remains unclear how exactly the 2021 PNW heatwave unfolded with such unprecedented magnitude, breaking temperature records by several degrees Celsius (Philip et al., in review).

During the devastating 2003 and 2010 heatwaves in Europe (Robine et al., 2008; Barriopedro et al., 2011), a multi-day heat accumulation took place; fueled by dry soils and hence strong surface heating, the atmospheric boundary layer (ABL) grew deeper and deeper and thereby entrained hot air from aloft (Miralles et al., 2014). For these and other compound hot and dry events, the relevance of both local and upwind drought conditions has already been highlighted (e.g., Fischer et al., 2007; Zampieri et al., 2009; Seneviratne et al. 2013; Hauser et al., 2016; Schumacher et al., 2019), enabling stronger land–atmosphere feedbacks that can intensify hot conditions (e.g., Zaitchik et al., 2006; Seneviratne et al., 2006a, 2010; Hirschi et al., 2011; Mueller & Seneviratne, 2012; Seneviratne et al. 2013; Stéfanon et al., 2014; Berg et al., 2014; Vogel et al. 2018). A large fraction of the PNW had unusually dry soils already in late spring (Ansah et al., 2021; Bumbaco et al., 2022), raising the question of what role soil moisture played during the heatwave. Further, given that the potent blocking system setting the stage for extreme heat below remains a marked feature of a meandering circumglobal jet stream (e.g., Rossby, 1939; Röthlisberger et al., 2014; Kornhuber et al., 2020), an open question is whether remote processes and interactions, for example instigated by anomalous sea surface temperatures (Feudale & Shukla, 2011; Wang et al., 2014) may have contributed to the 2021 PNW event. In fact, a recent study points to a developing cyclone south of Alaska, whose heat released by condensation in ascending air masses strengthened the Omega Block in the PNW in late June 2021 (Neal et al., 2022). While the positive anomaly in geopotential height at 500 hPa (Z500) was unprecedented in that region, this distinctive anticyclonic circulation pattern does not seem to explain the temperature escalations on its own (Philip et al., in review). Moreover, existing assessments of the human-caused exacerbation of this heatwave largely rely on statistical relationships derived from observations or based on physical simulations of the Earth System of the same region. However, it is not a priori clear whether they involve the same — potentially nonlinear (Philip et al., in review) — processes and interactions as those responsible for the PNW heatwave.

To address these questions, a factorial Earth System Model (ESM) approach is used here (Wehrli et al. 2018, 2019). In this approach different components of the Community Earth System Model (CESM; Hurrell et al., 2013) are either constrained or calculated interactively. Crucially, this framework includes simulations where the horizontal wind is nudged towards ERA5 data (Hersbach et al., 2020), so that the actual atmospheric circulation during the 2021 PNW heatwave is reproduced. As such, and since low-level winds are exempt from the nudging procedure and can freely interact with the surface, this framework provides insights into the possibly unique set of processes and interactions underlying this extraordinarily hot event. We begin our investigation with an assessment of the suspected drivers of the event, which can be conceptually separated into 'dynamic' and 'thermodynamic' (see, e.g., Wehrli et al., 2018 for further background). Here, we refer to the atmospheric circulation as the 'dynamic' component, whereas anomalous land and ocean surface states, as well as the background warming of the atmosphere and ocean since pre-industrial times, are related to 'thermodynamic' contributions. Building on this, we compare the dynamics of the 2021 PNW heatwave to observed and simulated events and highlight the occurrence of elevated temperatures throughout the entire troposphere. Next, using the atmospheric trajectory model TRACMASS (Aldama-Campino et al., 2020; Döös, 1995), driven with ERA5 data, we unravel the upwind heat budgets of anomalously hot air that was incorporated into the anticyclone, and isolate the effect of latent heating. Note that existing studies of upwind latent heat release focus primarily on the formation and maintenance of blockings (Pfahl et al., 2015; Steinfeld & Pfahl, 2019; Zschenderlein et al., 2020; Steinfeld et al., 2020; Neal et al., 2022), and hence on 'dynamic' aspects. Here, we follow a different approach and instead quantify the direct effect of upwind latent heating on downwind heatwave temperatures for the given large-scale circulation. While the causal link between upwind heat release and downwind state of the troposphere is established by the flow of air itself as well as processes occurring *en route*, which we approximate with backward trajectories, it is not a priori clear to what extent near-surface temperatures are affected. We also investigate whether other regions around the globe provide favorable conditions for an event with a similar anatomy as the 2021 PNW heatwave, and conclude our analysis with an outlook.

2 Materials and Methods

2.1 Defining the heatwave region

The heatwave region employed here, 45 °N–52 °N and 119 °W–123 °W, is the same as the area used for a rapid attribution study (Philip et al., in review). The area is close to—yet not centered on—the temperature anomaly epicenter, and instead contains the three most populous metropolitan areas (CIESIN, 2018) affected by the extreme heat: Portland, Seattle, and Vancouver.

2.2 The Community Earth System Model and disentangling framework

This study is based on global ESM simulations performed with CESM 1.2.2 spanning the time period from 1979 to 2021 and employs the method introduced by Wehrli et al. (2018, 2019). The disentangling framework rests on a set of simulations with interactively calculated or constrained components, i.e., the atmosphere (Community Atmosphere Model version 5.3, CAM5), land (Community Land Model version 4, CLM4) and ocean surface (always constrained). With this, we estimate the influence of physical drivers such as atmospheric circulation, soil moisture or

SST anomalies, as well as the long-term human imprint on the Earth system. The framework, now driven with ERA5 instead of ERA-Interim data where applicable, is described in detail by Wehrli et al. (2018, 2019), and an overview of how the different CESM components were forced here is provided in **Table 1**. In essence, the dynamic and thermodynamic contributions are determined by temperature anomaly differences in the heatwave region between simulations with differently forced components (e.g., actual vs. climatological soil moisture). Note that the first 3 simulation years until 1981 are discarded to allow for model spin-up. All anomalies presented in this study are calculated with respect to (w.r.t.) the climatological baseline period, 1982–2008, and **Fig. 1** depicts the disentangling framework used here with all employed CESM configurations.

	SST and sea ice	**Atmosphere**	**Soil moisture**
Reference (actual)	oF	aF	sF
Climatological (1982–2008)	oC	*aF | aI*	sC
Natural (1870–1890)	oN	aF | aFghgN	*sF*
Interactive	*oF*	aI	sI

Table 1: Overview of the different components used for analysis. The capitalized letter in each label (e.g., oF) indicates whether the respective component is constrained — or 'forced' — toward actual reference data (F), the 1982–2008 climatology (C), a natural scenario with removed background warming with respect to 1870–1890 (N), or calculated interactively (I). Selected combinations of these components are used here to unravel the roles of dynamic and thermodynamic drivers (**Fig 1)**. Italic font in gray indicates that a different component than suggested by the corresponding row is used; for example, a 'climatological' atmosphere is never constrained, and the atmosphere in simulations with climatological land and ocean surface states is thus either calculated interactively or nudged toward actual winds.

Following Wehrli et al. (2018), in all simulations, SSTs and sea ice are constrained with transient monthly observations, consisting of a merge of the Hadley Centre sea ice and SST dataset version 1 and version 2 of the National Oceanic and Atmospheric Administration (NOAA) weekly optimum interpolation (OI) SST analysis (Hurrell et al., 2008). Note that since the ocean is always forced in this study, for interactively calculated atmospheres, only (one-way) interactions rather than feedbacks between surface ocean state and large-scale atmospheric circulation are captured. Nevertheless, the winds in simulations with nudged circulation toward reanalysis data essentially represent the interplay of actual atmospheric internal variability and, e.g., ocean–atmosphere feedbacks. The employed solar and greenhouse gas (GHG) forcings, as well as atmospheric chemistry, aerosols and land-use change, are largely based on historical data. We refer to Wehrli et al. (2018) for details, and note that global CO_2, CH_4 and N_2O concentration observations were updated to cover the entire simulation period until the end of 2021.

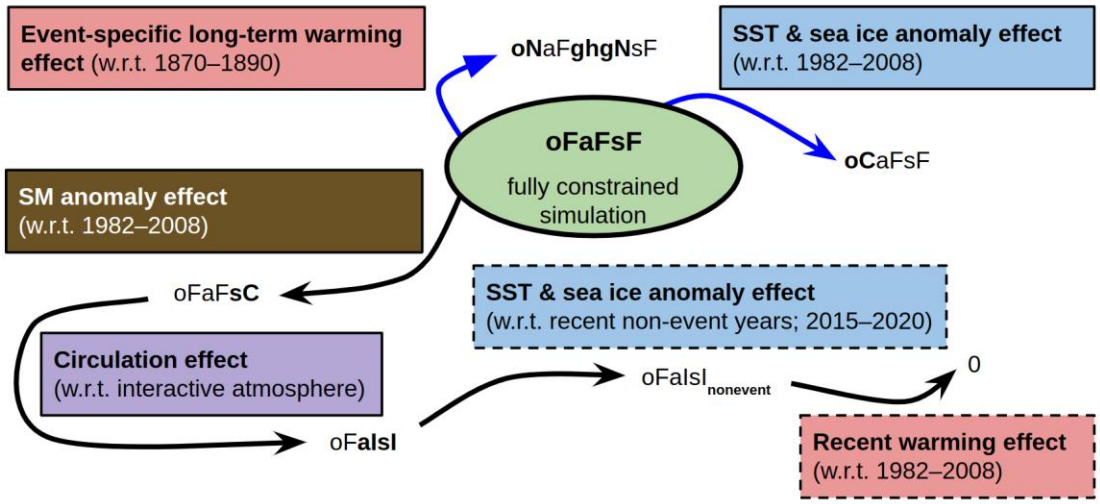

Fig. 1: Disentangling framework to estimate physical drivers of the heat wave. Black arrows denote contributions that are part of the additive disentangling framework presented by Wehrli et al. (2019), and indicate the pathway used to estimate the contributions of dynamic and thermodynamic drivers. For example, we start with the fully constrained simulation (oFaFsF) and compare it to a simulation with climatological soil moisture (oFaFsC); their temperature anomaly difference indicates the effect of anomalous soil moisture. Next, by comparing the simulation with climatological soil moisture to the ensemble mean of simulations where winds are calculated interactively, we obtain the circulation effect, and so on. Note that contributions estimated based solely on simulations with interactive atmosphere are considered to be 'generic' estimates (dashed border), contrary to 'event-specific' effects estimated with a constrained atmosphere (toward actual winds according to ERA5). All these heatwave contributions are displayed for the 2021 PNW event in **Fig. 2c**. Blue arrows indicate additional estimates of 'event-specific' ocean and long-term warming effects that are not part of the original additive framework.

2.2.1 Nudging of the atmospheric circulation

In this study, the atmospheric circulation is either calculated interactively, or 'nudged' toward reference data for each model level. For the nudging, CAM5's prognostic horizontal wind equations are extended by a nudging term that relaxes the wind field toward the reference, that is, the next 6-hourly reanalysis step for every model time step (30 minutes). The same vertical nudging profile as introduced by Wehrli et al. (2018) is used for the troposphere (**Fig. S1**), in which only the zonal and meridional winds above roughly 700 hPa are forced towards the reference, here consisting of 6-hourly ERA5 data regridded to CESM's 0.9° x 1.25° horizontal resolution. Note that even though vertical winds are never nudged, mass conservation as expressed, e.g., in the continuity equation, ensures that the grid-scale vertical motion, especially above 700 hPa, also approaches the reference dataset. Due to storage considerations, only the troposphere and lower stratosphere are nudged towards reanalysis data, while the four uppermost model levels — roughly corresponding to 3.6, 7.6, 14.3 and 24.6 hPa pressure levels — are calculated interactively. Note that the interactive calculation of upper model levels does not affect tropospheric winds.

2.2.2 Soil moisture

To assess the impact of the land surface state on the 2021 PNW heatwave, soil moisture is either constrained or calculated interactively in our disentangling framework, following the approach of Wehrli et al. (2019). In particular, we constrain 'actual' or 'climatological' (1982–2008) soil moisture values, but never force CESM with ERA5 soil moisture: a direct transfer of such a highly model-dependent quantity between different models should be avoided (Koster et al., 2009). Instead, we first use meteorological input from ERA5 to drive only the land surface model (CLM4) from CESM in offline mode. This produces an ERA5-driven soil moisture dataset that is consistent with the fully coupled model (CESM) in terms of, e.g., soil levels and texture (Koster et al., 2009). The technical implementation of the soil moisture prescription in CLM4 was performed and assessed by Hauser et al. (2017). As in Wehrli et al. (2019), soil moisture is only constrained when soils are not frozen. Otherwise, soil moisture is calculated interactively to avoid artificial ice generation and ensuing unrealistic ground heat fluxes (see Hauser et al., 2017 for details).

2.3 Composite analysis of strong anticyclones

To better understand the role of dynamics during the 2021 PNW heatwave, we compare it to other events characterized by strong anticyclonic circulation aloft. While anticyclones enabling extreme temperatures underneath are often described as quasi-stationary (e.g., Lau & Nath, 2012; Petoukhov et al., 2016; Yao et al., 2017; Kornhuber et al., 2020), the blocking high over the PNW slowly shifted eastward during the 2021 heatwave (see **Fig. S2a**). We thus employ an approach that is not bound to a static region, and instead track anticyclones in our fully constrained base CESM simulation (oFaFsF, see section 2.2). Specifically, we focus on events that occurred in similar latitudes as the PNW 2021 heatwave (45 °N–60 °N) over land and during boreal summer (JJA). Anticyclones are detected using the geopotential height at 500 hPa (Z500). First, a 15-day running mean of Z500 is calculated for every terrestrial grid cell in the selected latitudinal band, followed by the calculation of standardized anomalies w.r.t. 1982–2021 (Z500'). Strong positive anomalies indicate anticyclonic flow acting on timescales of several days, so we only retain areas where Z500' > 2σ, and then identify a Z500' peak location for all days on which the criterion is met. We proceed to select the maximum anomalies for all sets of consecutive days with a Z500' peak location, which yields several events in our domain every summer.

For these events, a rectangular domain with 3 different sizes — 6°x6°, 10°x10°, 20°x20° — is first centered on the respective peak location, given that the respective area-averaged Z500' exceeds 2σ. This additional filtering ensures that only events affecting large areas — in addition to lasting several days — are analyzed. We only show results for 10°x10° domains here, but this choice does not affect our conclusions. Iterative day-by-day tracking is initiated on the event's peak day and at the peak location, with anticyclone locations on the previous and subsequent day being assigned to Z500' maxima within 10°x10° areas centered on the peak location. Going

further back or forward in time, the respective previously identified anticyclone locations are used for centering the 10°x10° moving window. While some anticyclones may not be tracked properly due to the implied horizontal movement restriction, the focus here is on slowly moving anticyclones. Anticyclone peak locations are only identified over land, but anticyclone tracking is performed anywhere and without additional criteria for the 7 days before the peak, and also the 3 days after. The rationale here is that for the PNW 2021 heatwave, temperatures plateaued only after the anticyclone had reached its maximum intensity (Philip et al., in review). If any events overlap within this 11d-period, only the most intense one — again, based on Z500' — is retained. Finally, once all anticyclonic events have been identified and tracked in time, the corresponding area averages of several variables — such as temperatures at different pressure levels — are logged to enable a composite analysis. Since Z500 increases for a warming atmosphere (e.g., Sánchez-Benítez et al., 2017), we have repeated the entire analysis for linearly detrended Z500 data, and found that the decision whether to detrend does not noticeably affect our results and conclusions. As detrending is not necessary for the simulations with interactive atmosphere (see details below), we only show results obtained without prior linear trend removal.

After comparing the dynamics of the 2021 PNW heatwave to other anticyclonic events, we repeat the analysis for simulations with fully interactive atmospheres. Due to storage constraints, all the required data are only available from 2009 onward, and hence the analysis is restricted to 2009–2021, which also serves as the climatological base period. This represents the sole methodological difference between the anticyclone comparisons of simulations with nudged and with interactive atmospheres. The limited time period renders detrending obsolete, and is more than compensated by the use of many ensemble members (80 each for oFaIsI and oFaIsF).

2.3.1 Simulation with flat terrain

To assess the impact of mountainous terrain in the PNW on surface–atmosphere interactions, and in particular maximum ABL heights, we conduct a CESM simulation identical to the fully forced setup (oFaFsF), except that the mean grid cell height over land between 20 °N –70 °N and 180 °W–80°W is set to the heatwave region mean height. Subgrid-scale surface roughness parameters are left unchanged, that is, we only investigate the impact of mountains at the grid-scale or larger.

2.4 Backward trajectory analysis of hot events

Motivated by the presence of anomalously high temperatures throughout the troposphere above the PNW during the 2021 event, we were interested in the origin of this heat anomaly and how the 2021 PNW compares to other North American heatwaves. Therefore, we first identify additional heatwaves over most of North America, and then track the air involved in those hot extremes back in time. By doing so, we not only unravel where the air that enabled unprecedented temperature escalations in the PNW came from, but we can also compare if this

air was primarily hot because of its origin, or perhaps due to heating processes occurring *en route*.

2.4.1 Defining hot events

Hot extremes are identified for land areas within North America, latitudinally restricted from 30°N to 60°N. For every summer (JJA) from 1982 to 2021, the day with most land grid cells for which their maximum temperature (TX) equals the respective ERA5 record value since 1982 (TXx_x) is chosen. The event location is then determined by the highest TX anomaly among these pixels. If there are no record-temperature grid cells in an entire summer, the date on which most pixels satisfy $TX > TXx_{90th\ perc.}$ is chosen, that is, the all-time record temperature TXx_x, is replaced by the 90th percentile of TXx. If necessary, the quantile further decreases in steps of 10% until an event is found. No other event is allowed to occur within +/- 7 days. This procedure is performed four times every year, so that there are 4x40=160 events, one of which being the 2021 PNW heatwave.

2.4.2 Tracking air back in time with TRACMASS–ERA5

To follow the evolution of the air masses of the hot events backwards in time, we employ the Lagrangian trajectory model TRACMASS v7.0 (Aldama-Campino et al., 2020; Döös, 1995), which can be applied to study both the atmospheric or oceanic circulation (e.g., Dey et al., 2020; Liang & Xue, 2020). TRACMASS essentially converts reanalysis or General Circulation Model (GCM) winds into 3D mass transports between grid boxes by solving the continuity equation. As a consequence, the resulting trajectories are mass conserving, and at the grid-scale or larger scales, consistent with the input circulation (Döös et al., 2017). Here, TRACMASS is employed to calculate ERA5-based 10-d backward trajectories, using 6-hourly horizontal winds at 0.5° x 0.5° on hybrid model levels and surface pressure. We largely follow the IFS setup (provided by the authors of TRACMASS, and accessed on November 25, 2021 through https://www.tracmass.org) for 6-hourly ERA-Interim input data, using the time-step scheme with 120 iterations between model time steps. The release of about 6’000 air parcels — conceptualizations of coherent air masses — for each hot event is configured as follows: for a 3°x3° area centered over each identified heatwave (see details above), air parcels are released 5 times (every 6 hours on the peak day of the hot event, i.e., 00, 06, 12, 18 UTC, and on 00 UTC of the following day). These parcels are seeded on a vertical wall (isec=3), with each particle reflecting the air mass at the respective time (nqua=3). About 3 to 4 parcels are seeded in each selected grid box (partquant=50). This is performed such that air parcels residing over the center of each hot extreme, between 675 hPa and 475 hPa, can be tracked backwards in time for at least 10 days. The pressure range of 475 hPa–675 hPa was chosen for two reasons; first, it corresponds to tropospheric air that is likely to interact with a (potentially deep) ABL underneath, and enables a nearly analogous analysis for trajectories driven by CESM (see section 2.5) with far fewer model levels, two of which roughly cover this range (temporally averaged

over flat terrain: 482 hPa–652 hPa). In addition to air parcel positions, we also trace the specific humidity and temperature to perform further analyses.

We note that, again motivated by storage considerations, we use temporally limited (6-hourly) and vertically incomplete ERA5 data on the lowermost 98 model levels (instead of the full 137, which cover the entire stratosphere and even most of the mesosphere). The 98 levels suffice, however, to track air parcels released in the middle and lower troposphere back in time for 10 days. Nevertheless, we compared trajectories calculated as described above, and repeated the calculation for the 2021 PNW heatwave using hourly ERA5 input at 0.25 x 0.25 horizontal resolution and at all 137 vertical levels, and found only minor differences (not shown). This also holds for backward day -10, when trajectory errors are expected to be greatest, since they accumulate in the direction of integration (e.g., Stohl & Seibert, 1998).

2.4.3 Diagnosis of latent heating along trajectories

Even though hot events are exclusively diagnosed based on temperature here, many of them are associated with anticyclonic circulation aloft, which implies adiabatic warming due to subsidence particularly in the last 72 hours (Zschenderlein et al., 2019). While this adiabatic heating — converting potential into kinetic energy — is often considered to be a key driver of high near-surface temperatures in the midlatitudes (e.g., Bieli et al., 2015), it cannot explain the presence of high potential temperatures in the upper troposphere such as witnessed during the 2021 PNW event (see **Fig. S2b**). Therefore, to investigate the unprecedented free tropospheric heat during the 2021 PNW heatwave, we consider the *initial state* of air 10 days prior to arriving, and processes occurring *en route* that shape the *final state* (above the respective hot extreme). Specifically, we unravel the potential temperature budgets of all North American hot events including the recent PNW heatwave, and differentiate between diabatic heating and cooling. In addition, we also diagnose latent heat release as a particular kind of diabatic heating.

In practice, we employ a processed-based approach (Sodemann et al., 2008; Keune & Miralles, 2019) to estimate latent heating along air parcel trajectories. The underlying rationale is that if a specific process (e.g., radiative cooling) dominates within a 6-hourly trajectory step, this is reflected in a change of state (e.g., decreasing potential temperature, conserved specific humidity). From the perspective of an air parcel, latent heating should be accompanied by a rise in potential temperature while the equivalent potential temperature — that is conserved even for vertical motion including condensation — should remain roughly constant (or decrease due to dry air entrainment). We note that the trajectory calculations are imperfect, and associated inaccuracies, interpolation errors as well as numerical imprecision can cause noise (Sodemann et al., 2008). Therefore, we employ three sets of increasingly strict criteria to determine latent heating; loose, moderate and strict. For all of these, we require the 6-hourly potential temperature change to be positive. We also enforce a relative humidity (RH) criterion; the RH must exceed either 70%, 80% or 90% at the beginning or end of a 6-hourly time period. Furthermore, the

equivalent potential temperature increase is limited to 2 °C, 1 °C or 0 °C. This results in three progressively conservative estimates of latent heating; unless specified otherwise, results are shown for the moderate criterion (80% relative humidity required, and a maximum equivalent potential temperature increase of 1 °C).

2.5 Exploring the impact of upwind latent heating on downwind temperatures with CESM

The analysis of TRACMASS–ERA5 trajectories enables an insight into the upwind diabatic heating budgets of hot events. However, it cannot provide an accurate estimate of the causal link between upwind latent heating and downwind heatwave temperatures – especially since the diagnosis of latent heating requires assumptions and associated parameter choices (see above). To this end, we first repeat the backward trajectory calculation with TRACMASS as described above, but use CESM output (oFaFsF) as a forcing instead. The only notable technical differences to TRACMASS–ERA5 are introduced by different horizontal and vertical input resolutions, hence fewer air parcels are released for otherwise unchanged settings. Next, having verified that the PNW 2021 heatwave backward trajectories are largely consistent between ERA5 and our base (or fully forced, i.e. most realistic) CESM run, we perform additional simulations to estimate the heatwave temperature impact of remote latent heating. Since trajectory analyses, whether forced directly by ERA5 or by ERA5-driven CESM data, reveal a predominantly oceanic origin of PNW 2021 heatwave air 10 days prior to arrival, latent heating is controlled in a large domain within the North Pacific Ocean (20 °N–60 °N, 120 °E–240 °E). In practice, we artificially increase or decrease specific humidity within the oceanic part of the domain, which results in less moisture being available for condensation and ultimately precipitation, our proxy for latent heating.

Considering that the lower troposphere contributes most of the moisture for precipitation (e.g., Sherwood et al., 2010), which is only partly affected by the default nudging procedure below ~700 hPa (section 2.2.1), we set up a new reference simulation, also fully forced (like oFaFsF), but with nudged specific humidity — in addition to horizontal winds —throughout the entire troposphere. This results in similar PNW 2021 heatwave temperatures as in our base simulation obtained for the vertical nudging profile (**Fig. S1**) and without humidity-nudging (**Fig. S3a**), and is used as a reference for other simulations with a modified vertical specific humidity profile. The latter are obtained by artificially increasing and lowering the values of 6-hourly specific humidity fields used for nudging, only within 500 hPa–800 hPa and the North Pacific domain from June 19 to 26, using several scaling factors ranging from 0.5 to 1.25. This procedure acts to increase or decrease precipitation, but we refrain from attempting to fully suppress precipitation within our domain for multiple reasons. Enforcing dry air in proximity to the surface results in unrealistically deep marine ABLs and affects the surface energy partitioning; also, humidity is controlled only every 6 hours while the model has timesteps of 30 minutes, so that moisture can still be gained by surface evaporation or enter the domain horizontally. Even more importantly, since all these experiments rely on the actual atmospheric

circulation, enforcing a 'climatological' — or any other reference — precipitation field would not yield a physically coherent simulation. Instead, we use a set of experiments with moderately altered latent heating to gauge the sensitivity on PNW 2021 heatwave temperatures. To the authors' knowledge, such an estimate has not yet been presented, even though the importance of upwind latent heating for downwind dynamics has long been noted (Hoskins et al., 1985; Davies et al., 1993; Stoelinga, 1996; Pfahl et al., 2015; Steinfeld & Pfahl, 2019; Zschenderlein et al., 2020).

2.6 Upwind latent heating beyond North America

Lastly, the analyses of TRACMASS–ERA5 backward trajectories described in sections 2.3 are extended to other continents: South America, Europe (defined as 37.5 °N–62.5 °N, -15 °E–50 °E), and Australia. We employ the same hot event definition as for North America and investigate all summer seasons from 1982 to 2021; since our focus is on mid-latitudinal climates, we use JJA and DJF for boreal and austral summer, respectively. Note that for Australia, only 2 (instead of 4) hot events per year are evaluated here.

3 Results

3.1 Record-shattering temperatures and their physical drivers

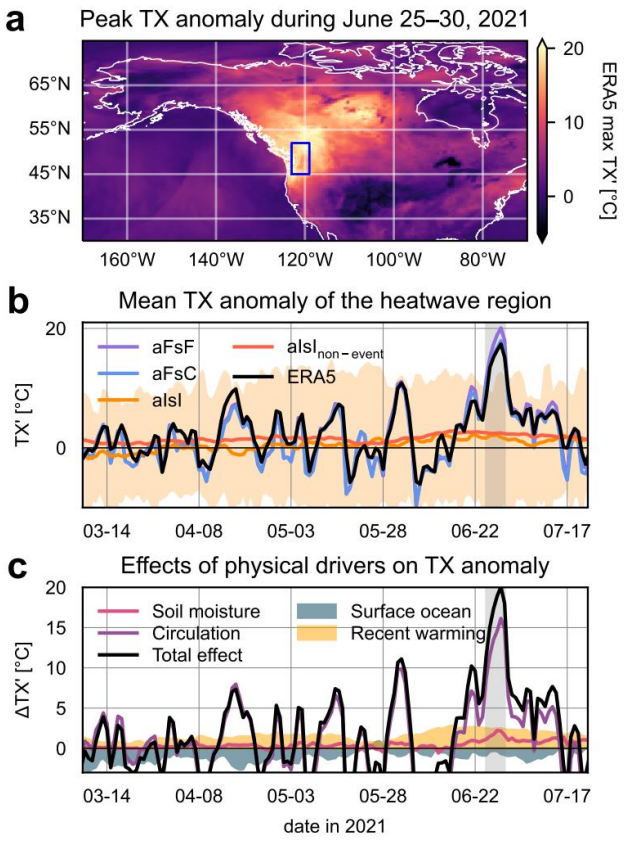

Fig. 2: Unprecedented temperature anomalies in late June 2021 in the Pacific Northwest. (a) Highest daily maximum temperature anomaly reached in ERA5 from June 25 to 30, 2021. During these last days of June, the event reached its peak intensity in the heatwave region used throughout this study (blue contour). Anomalies are calculated with respect to 1982–2008. **(b)** Anomaly timeseries for the heatwave region, depicting area-weighted mean daily maximum temperatures from ERA5 (black line). In addition, multiple simulations from CESM are shown: the 'reference' — fully constrained atmosphere and soil moisture (aFsF; purple), same but with constrained climatological soil moisture (aFsC; blue), and interactive atmosphere and soil moisture (aIsI; orange). The latter consists of 80 simulations, whose ensemble mean is indicated by a solid line, while the shading visualizes minima and maxima. The ensemble mean of aIsI simulations for recent non-event years (2015–2020) is also shown. **(c)** Physical drivers in the additive disentangling framework (**Fig. 1**), obtained by TX' differences visualized in (b). The sum of these contributions is equal to TX' indicated by the fully constrained simulation.

In the last days of June 2021, much of the Pacific Northwest experienced near-surface ERA5 reanalysis temperature anomalies approaching—and even exceeding—20°C with respect to 1982–2008 (**Fig. 2a**). Averaged across the heatwave region (blue contour in **Fig. 2a**) and according to ERA5 data, the daily maximum temperature anomaly peaks at more than 17°C on June 29 (**Fig. 2b**; black line) following a sharp increase after June 25. Our base simulation from

the heat disentangling framework with constrained oceans, soil moisture as well as mid- and upper-level tropospheric winds, named '(oF)aFsF', slightly overestimates the event's magnitude. Nevertheless, the simulated heatwave portrays a realistic temperature evolution. This is also the case for the simulation with climatological—rather than actual—prescribed soil moisture (aFsC). The remaining model simulations visualized here feature an interactive atmosphere and soil moisture (aIsI) and consist of 80 ensemble members. None of these simulations produced a heatwave that could rival the actual event; in this region and for late June 2021, even the ensemble maxima (colored shadings) are roughly 7°C less hot than the base simulation (aFsF). This not only emphasizes the key role of the atmospheric circulation, but also highlights the need to understand the full set of drivers involved in the occurrence of this remarkable hot extreme.

Thus, using the presented set of simulations and the additive disentangling approach introduced by Wehrli et al. 2019 (see also Methods and **Fig. 1**), the effects of several physical drivers are estimated (**Fig. 2c**). The effect of soil moisture is about 2°C during the peak of the event, while the circulation effect peaks at a remarkable 16°C. Sensitivity experiments indicate that the initial soil moisture state prior to the event only played a minor role (< 0.5 °C), implying that the total soil moisture contribution was largely enabled by desiccating soils during the heatwave (**Fig. S4a**). Among the two remaining drivers in our additive framework, the effects of anomalous SSTs (with respect to the mean state of 2015–2020) and of our changing climate (compared to 1982–2008), only the latter acted to amplify the event's magnitude. Averaged over June 25–30, the soil moisture effect amounts to 10.3%, while the circulation explains 78.6%. The remaining event magnitude is attributable to anomalous ocean surface state (-0.6 °C or -3.5%) and recent warming (2.5 °C or 14.6%). We point out that these surface ocean and recent warming effects are obtained from simulations in which the atmosphere is calculated interactively and are hence 'generic' estimates, unlike the 'event-specific' soil moisture and circulation effects derived from constrained winds. According to additional simulations, the event-specific effect of long-term warming since 1870–1890 amounts to about 1.4 °C during the last 6 days of June 2021 (**Fig. S4b**). Our estimates of anthropogenic influence thus clearly depend on whether we analyze many simulated events in the same region (+2.5°C w.r.t. 1982–2008), or the actual PNW heatwave with its characteristic circulation pattern (+1.4°C w.r.t. 1870–1890), but both approaches point to an exacerbating impact of the warming climate. Meanwhile, the event-specific contribution of anomalous surface ocean state with respect to 1982–2008 is merely 0.2 °C. Based on our analysis, the 2021 PNW heatwave should thus be seen as largely enabled by dynamics (that is, the atmospheric circulation), yet significantly exacerbated by thermodynamic drivers—particularly dry soils but also the warming climate, while surface ocean anomaly effects as defined here are negligible. We point out that the same limitations as already mentioned for soil moisture, i.e., ocean–circulation feedbacks cannot be targeted within our framework, also apply here and hence the true roles of land and ocean surfaces may be underestimated. Regardless of potential underlying interactions, the atmospheric

474 circulation during the event — colloquially referred to as 'heat dome' — deserves further
475 investigation.

476 ***3.2 Comparing the dynamics to other strong anticyclonic events***

477 To better understand the dynamics of the PNW 2021 heatwave, we begin with a
478 comparison to other historical events characterized by strong anticyclonic circulation patterns.
479 Specifically, we track anticyclones in all summers (JJA) from 1982 to 2021 between 45 °N–60
480 °N, using a horizontal extent of 10° x 10° (see Methods for details). All events are identified
481 based on standardized anomalies of the geopotential height at 500 hPa (Z500') above 2σ, and
482 results are visualized with respect to the timing of the Z500' peak. For the 2021 PNW heatwave,
483 the associated near-surface daily maximum temperature anomaly (TX') culminates two days after
484 Z500', and trumps every other event since 1982 (**Fig. 3a**). Similarly, the peak in Z500' during
485 the 2021 PNW heatwave (pink lines in **Fig. 3a**) is unprecedented. As one would expect, events
486 whose TX' during and shortly after the respective Z500' peak is lower than most others (blue
487 lines) are also associated with a weaker Z500' compared to hotter events (orange lines). But
488 events with the highest near-surface temperatures are also associated with temperature anomalies
489 that extend throughout the troposphere; in the case of the 2021 PNW heatwave, the air at 500
490 hPa was already hotter than for any other anticyclonic event analyzed here. Of course, positive
491 temperature anomalies aloft are to be expected in light of the anticyclonic flow and associated
492 subsidence, which explains why temperature anomalies strongly increase in magnitude from the
493 upper (approximated by 250 hPa) to the lower troposphere (850 hPa). Nevertheless, the presence
494 of warmer-than-usual air even far aloft indicates that it not only matters how quickly the air is
495 forced to sink (and consequently experience adiabatic heating), but also what initial state the air
496 has even before it spirals downwards.

497 Next, we extend the analysis to simulations based on fully interactive atmospheres (**Fig.**
498 **3b**). As for the actual events simulated with nudged circulation, higher near-surface temperatures
499 are associated with stronger anticyclones, and temperature anomalies extending throughout the
500 troposphere. This suggests that the tropospheric temperature evolution during the actual 2021
501 PNW event — visualized separately for our heatwave region in **Fig. 3c** — is more than the mere
502 manifestation of strong atmospheric subsidence. Before investigating this further, we emphasize
503 that a hot free troposphere alone does not guarantee extreme near-surface temperatures. Already
504 recognized for other mega-heatwaves in the midlatitudes, a so-called multi-day 'heat buildup'
505 can occur in ABLs several kilometers deep (Miralles et al., 2014). ABL growth is mostly
506 controlled by surface heating, but also dependent on numerous land–atmosphere interactions and
507 actually hindered by subsidence aloft (e.g., Troen & Mahrt, 1986; Rey-Sanchez et al., 2021). As
508 depicted in **Fig. 3c** and mandated by atmospheric stability considerations, the potential
509 temperature at 500 hPa is hotter than at 850 hPa and at 2m above the ground, even with respect
510 to near-surface daily maximum temperatures. Considering this and that a growing ABL implies
511 that a lot of previously 'free tropospheric' air is incorporated, even hotter air is entrained for

deeper ABLs. This, in turn, also implies higher near-surface peak temperatures due to strong daytime vertical mixing.

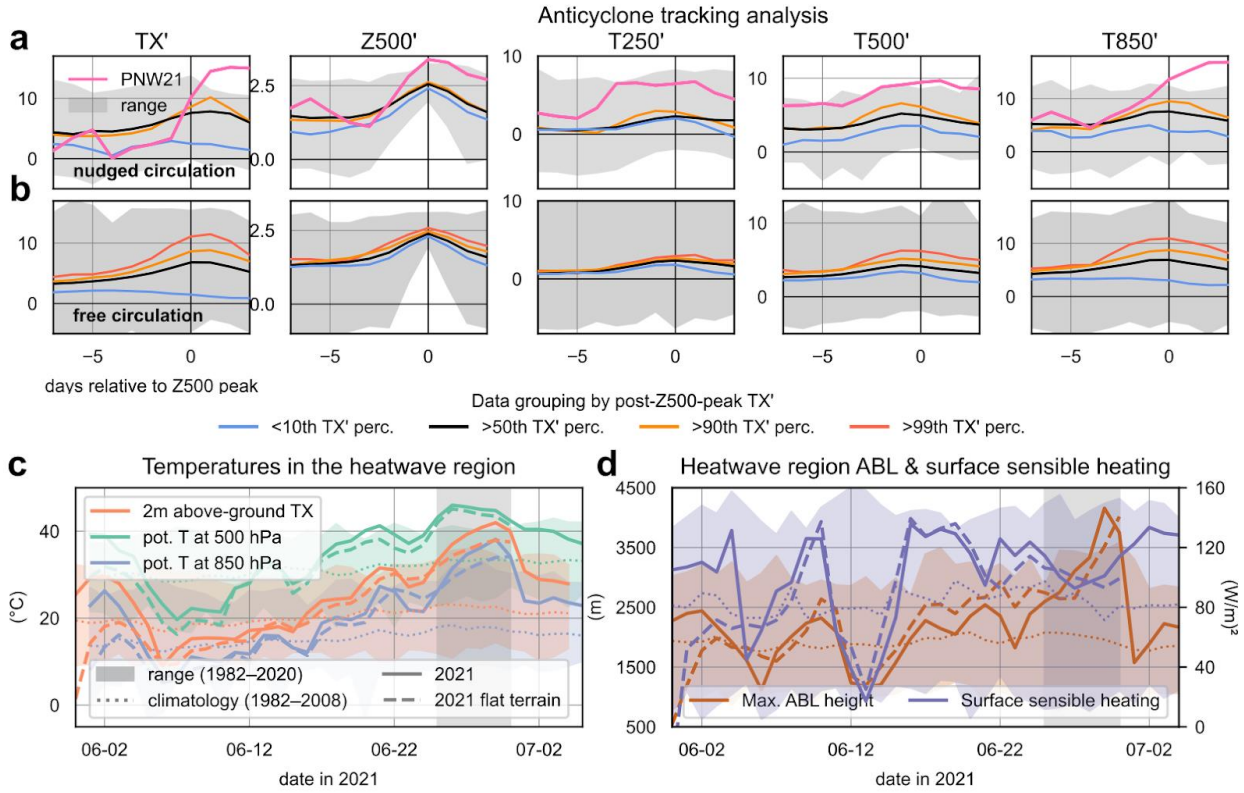

Fig. 3: Investigating the dynamics of the 2021 PNW heatwave with CESM. **(a)** Results for nudged atmospheric circulation, with near-surface temperature anomalies, Z500 anomalies, and temperature anomalies in the upper, middle and lower troposphere (from left to right). All data are based on a 10°x10° domain centered on the respective anticyclone position and are plotted with respect to the day of peak Z500 intensity. A range excluding the PNW 2021 event (pink line) indicates previous minima and maxima. In addition, events are grouped based on their near-surface heat anomaly, or more specifically, several TX' percentiles (10^{th}, 50^{th}, 90^{th}) after the Z500 peak. **(b)** As (a), but based on simulations with interactive atmosphere and soil moisture. The 99^{th} TX' percentile group is visualized along with the same data groups already employed for (a). **(c)** Temperatures in the heatwave region close to the surface, and the potential temperatures at 850 and 500 hPa (defined here as the temperature that air would have if brought adiabatically to 2m above ground), from the base CESM simulation with nudged winds. Data are presented for the actual 2021 event (solid lines), as a range for previous years since 1982, and as the climatological mean (dotted lines). Temperatures for an otherwise identical simulation with flat terrain in western North America are also indicated (dashed lines). **(d)** As (c), but showing the daily maximum ABL height and mean surface sensible heat flux instead.

In light of this, it is not surprising that during the 2021 heatwave, existing ABL height records were easily broken in our modeling framework with nudged circulation (**Fig. 3d**, orange line vs. shading). Interestingly, however, surface sensible heating (purple line) was not even close to previous maxima between 1982 and 2020, and even declined throughout most of the strong ABL growth. The latter is likely the consequence of sharply rising near-surface air temperatures, and raises the question how such a deep ABL could establish itself over the

heatwave region and surrounding areas (not shown) if not driven by an exceptional surface sensible heat flux. One potential key aspect relates to the topography of the Pacific Northwest; ABLs over mountain ranges in dry climates often grow deeper than over flat terrain, with depths of 2 km or even 3 km (De Wekker & Kossman, 2015). We thus performed an additional CESM simulation, also with nudged winds and constrained soil moisture but without any (grid-scale) mountains in the entire Pacific Northwest. The resulting ABL in this experiment is deeper throughout most of June, but does not grow as rapidly towards the end of the month as in our base simulation (dashed vs. solid orange lines), and is hence several hundred meters less deep during peak heat. Consequently, and despite initially stronger surface sensible heating in our simulation without mountains, less heat is entrained from aloft, even though the temperatures at 500 hPa remain largely similar (**Fig. 3c**, dashed vs. solid green line). Further below, however, a temperature difference of several degrees Celsius emerges (dashed vs. solid blue and orange lines), suggesting that the terrain in the PNW acted to significantly amplify heatwave temperatures by enabling strong and rapid ABL growth.

3.3 Unraveling the role of upwind latent heating

While this additional experiment provides evidence for a strong interplay between the Earth's surface and atmosphere in the PNW, it remains unclear why the upper troposphere — where adiabatic heating through subsidence is more limited than at lower levels — was anomalously hot. Also, compared to other North American hot events (see Methods), the anticyclone intensity (gauged by Z500') during the 2021 mega-heatwave alone does not account for the extreme near-surface temperatures, unlike tropospheric temperatures (gauged by T500'), and Z500' is also not sufficiently extreme to 'explain' T500', contrary to many other events (**Fig. S5**).

Therefore, in a next step, air residing over the PNW during the peak of the heat is tracked back in time for 10 days using ERA5 data (see Methods for details). This unravels the history of heatwave air, depicted as a function of time and height (**Fig. 4a**) and of latitude and longitude (**Fig. 4b**). In the last few days prior to peak heat, from June 25, the air masses were already part of a strengthening anticyclone (red and orange colors in **Figs. 4a–b**), and hence mostly subject to slowly descending vertical motion. Before becoming part of the anticyclone, the air crossed the entire Pacific Ocean, with a large amount of tracked air parcels originating in the lower troposphere in the tropical West Pacific. This is why, compared to other hot events in North America (Methods), the initial state of the air is characterized by a rather high mean temperature and pressure, but not potential temperature (red lines in **Fig. 4c**). Enabled by this tropical origin, the air that ultimately contributes to the 2021 PNW heatwave also had a higher specific humidity content than any other event analyzed here, only rivaled by a heatwave in 2015 (green lines in **Fig. 4c**). Given this initial state, what happened *en route,* that is, between the tropical West Pacific and the Pacific Northwest? As indicated by the mean temperature and pressure decrease, and consistent with the vertical analysis (**Fig. 4a**), backward days -10 through -6 are dominated

by comparatively rapid ascending motion, whereas in the last few days prior to arrival, the air descended and was heated adiabatically in the process. While this commenced earlier than for the 2015 event with a similar initial state, the intensity of adiabatic heating is far from unprecedented; other events such as in 1988 (orange lines in **Fig. 4c–d**) portray even stronger sinking motion shortly prior to arrival over the respective heatwave region. What makes the 2021 PNW heatwave unique, however, is the potential temperature evolution prior to backward day -5, coinciding with a pronounced decrease of specific humidity: our analysis indicates that the future heatwave air was subject to exceptional latent heating.

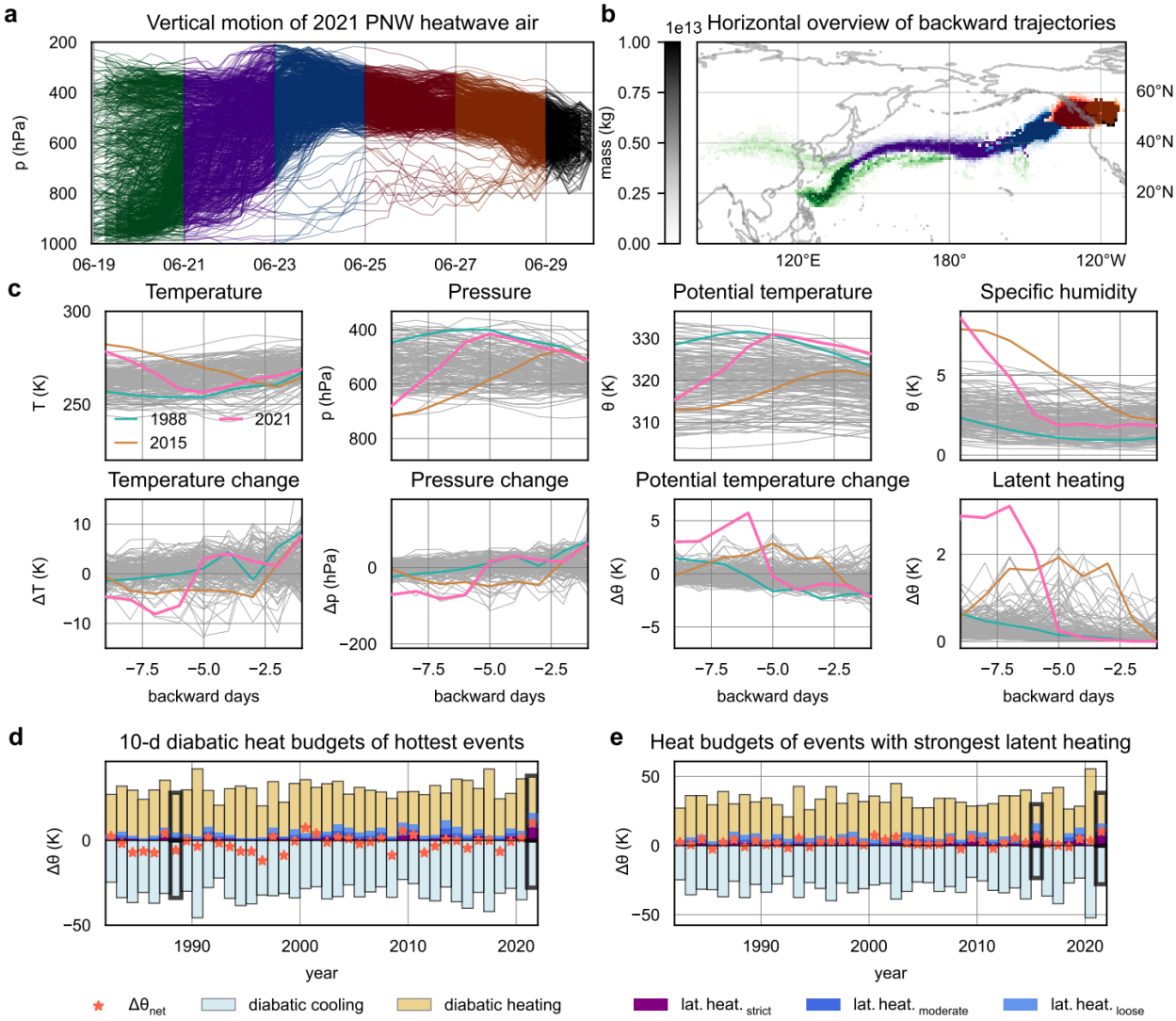

Fig. 4: Backward trajectory analysis of the PNW 2021 heatwave and other North American hot events. (a) Vertical backward analysis of air residing over the heatwave region in late June 2021, with colors marking different time periods. For aesthetic reasons, only 1000 randomly selected trajectories are shown. **(b)** Horizontal overview of backward trajectories, expressed as gridded air mass and colored consistently with the time dimension in (a). **(c)** Evolution of temperature, pressure, potential temperature and specific humidity for the air involved in North American hot events (gray lines in the upper row),

averaged over all respective backward trajectories. The 2021 PNW heatwave (red), as well as events in 1988 (orange) and 2015 (green) are emphasized (thick lines with markers). The lower row displays temporal changes of the same variables as displayed above. **(d)** Trajectory-averaged diabatic heating budgets of the most intense hot extreme for every summer since 1982. In addition to diabatic heating, cooling and the resulting net change in potential temperature (w.r.t. backward day -10), estimates of latent heating for 3 sets of criteria (see Methods) are depicted. The 1988 and 2021 PNW heatwaves are highlighted (thick black edges). **(e)** Like (d), but showing the hot event with strongest upwind latent heating for each year. The 2015 and 2021 PNW events are highlighted.

This result further emphasizes the role of upwind latent heating, whose influence on the dynamics has already been analyzed by Neal et al. (2022). The latter also suggested that the unusual tropospheric warmth originated in lower latitudes, and that it was possibly enhanced by heat released from condensation on the way to the PNW. Our trajectory analysis indicates that, while the air indeed largely originated in low latitudes, namely the tropical West Pacific (green grid cells in **Fig. 4b**), the intense latent heating *en route* strongly shaped the final state over the PNW. Specifically, the brunt of upwind heat release occurred in two warm conveyor belts, i.e., slantwise ascending air streams in the warm sector of extratropical cyclones (e.g., Browning, 1986; Schäfler & Harnisch, 2015), to the southeast of Japan and south of Alaska. This finding is consistent with the notion of remote and nearby ascending heating branches (with respect to a blocking) by Zschenderlein et al. (2020). Even for the 2015 event, whose air also mostly originated in the tropical West Pacific (not shown), latent heating of ascending air masses was clearly less intense than in 2021 until backward day -6. We note that our diagnosis of latent heating is subject to uncertainty and is performed thrice with increasingly strict criteria (see Methods), and of course, the net potential temperature change along the trajectories also depends on other sources of diabatic heating — most notably surface interactions — and cooling. Based on the mean trajectory heating budgets of the hottest event for every summer from 1982 to 2021 (**Fig. 4d**), strong diabatic heating (orange shading) is typically counteracted by even stronger cooling (light blue shading), and hence the net change *en route* often consists of cooling by several degrees Celsius (red stars). The air masses that ultimately participated in the 2021 PNW heatwave, on the other hand, experienced more intense latent heating (blue and purple shadings) than any other event analyzed here, which arguably enabled the unprecedented mean net heating rate of about 5 °C. Indeed, if the event with the most upwind latent heating per year — rather than the hottest (**Fig. 4d**) — is displayed, as in **Fig. 4e**, a clear majority of the net potential temperature changes is positive. This suggests that latent heating, even if not usually dominating the overall diabatic heating budget according to our diagnosis approach, assumes an important role in determining whether air gains or loses heat *en route* to the heatwave region, and hence ultimately affects downwind heatwave temperatures. This is confirmed for the 2021 PNW heatwave by additional CESM experiments (see Methods), for which the specific humidity, and hence precipitation and latent heating, was artificially reduced or enhanced from June 19 to 26 over the Northern Pacific. The results indicate a downwind daily maximum temperature sensitivity to upwind precipitation on the order of several degrees Celsius (**Fig. S6**).

3.4 Upwind latent heating around the globe

In the last part of the study, we attempt to clarify whether the PNW coincidentally served as a stage of extreme heat, or instead fostered the temperature escalations. Moreover, we explore whether there are any hotspots around the globe that might give rise to events with similar anatomies. To do so, we extend our trajectory analysis to a total of four regions — North and South America, Europe and Australia — and compare the intensity of upwind latent heating for numerous heatwaves (see Methods for details). These four regions show distinct patterns in upwind latent heating for the analyzed events in the 1982-2021 time period (**Fig. 5a**). In particular, the southeastern United States is particularly devoid of notable upwind latent heating, unlike northeastern North America. Nevertheless, air masses with the most intense latent heating exclusively contributed to heatwaves in the PNW, such as in 2021 but also others, and the entire northwestern coast features events where latent heating played a role. In South America, air masses involved in heatwaves frequently experience condensation, and in some cases, the associated heat release easily rivals the 2021 PNW event. Nevertheless, a direct comparison is not straightforward: even though heatwaves in the subtropics — in South America and also elsewhere, e.g., southern Europe — have been linked to anticyclonic circulation aloft, they are typically caused by displacements of subtropical high pressure systems (Sousa et al., 2018; Geirinhas et al., 2018) rather than blocking highs. As such, they are associated with different dynamics. In addition, our temperature-centered approach is designed for dry events with unusually high temperatures such as the 2021 PNW mega-heatwave, but does not capture humid heatwaves that commonly occur in tropical climates. We thus focus on heatwaves in the extratropical regions of South America, such as the upwind latent heating hotspot close to the Pampas. In Europe, nearly all analyzed events exhibit considerably weaker upwind latent heating compared to the PNW, generally remaining below 5 °C even along the northwestern coast of Europe and the British Isles. Only for two events in the North Caucasus, the heat released by condensation was comparable to the 2021 PNW heatwave, with up to 10 °C. No such event was found in Australia, where the strongest upwind latent heating occurs predominantly at the northern coast.

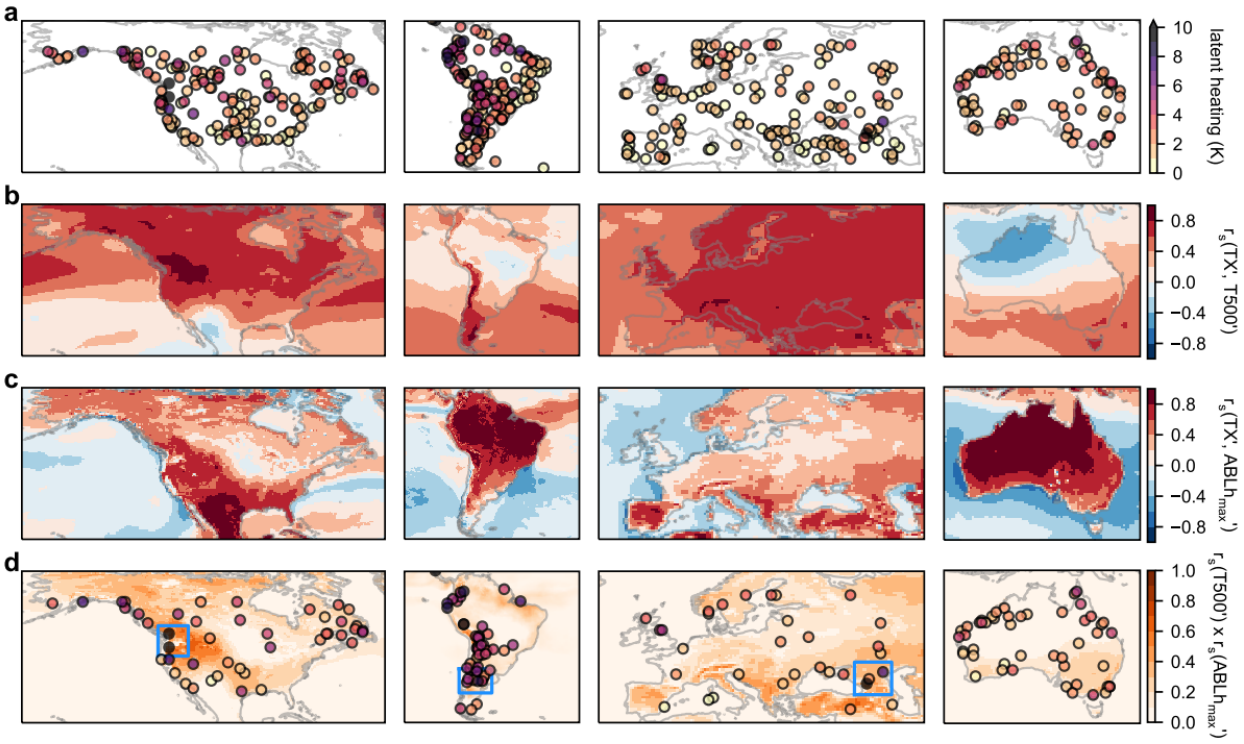

Fig. 5: Upwind latent heating prior to downwind heatwaves. (a) Upwind latent heating of summer heatwaves from 1982 to 2021 for North and South America, Europe and Australia, determined with TRACMASS–ERA5. **(b)** Correlation coefficients of ERA5 daily maximum near-surface and mean 500-hPa temperature anomalies; based on JJA for North America and Europe, and DJF for South America and Australia, 1982–2021. **(c)** As (b), but for the correlation of near-surface maximum temperature and maximum ABL depth. **(d)** Upwind latent heating of air masses from (a) that experience net diabatic heating in the 10 days prior to arrival over the respective heatwave region. The orange shading visualizes the product of (b) and (c), and indicates regions where hot summer days are frequently accompanied by anomalously deep ABLs and above-normal 500-hPa temperatures. The highlighted areas (PNW, Pampas, North Caucasus) are potentially favorable for the occurrence of heatwaves with a similar anatomy as the 2021 PNW event.

Having identified the several hotspots of intense upwind latent heating in different regions around the world, we now assess the link between near-surface daily maximum and 500-hPa temperatures (**Fig. 5b**). By doing so, we aim to delineate regions where summertime temperatures are frequently related to the state of free tropospheric air, which in turn largely depends on the prevailing large-scale circulation pattern, but also upwind processes such as surface and latent heating. Strong positive correlations are predominantly found in the midlatitudes, and hence over most of North America and Europe, yet only in the southern parts of Australia and South America, with the exception of the Andes. For peak near-surface temperatures and ABL heights (**Fig. 5c**), strongly positive relationships are found in the tropics and subtropics, while higher latitudes generally exhibit more moderate correlations. Even though these maps indicate mean relationships rather than drivers of individual events such as in 2021, the PNW stands out as a region where high near-surface temperatures are frequently accompanied by deep ABLs and elevated 500-hPa temperatures. This is visualized in **Fig. 5d**, where the mapped colors indicate the product of the correlation coefficients of the near-surface

daily maximum temperature with 500-hPa temperature (**Fig. 5b**) and ABL height (**Fig. 5c**) — values close to 1 indicate that hot extremes often coincide with both a heated troposphere and deep ABLs, as was the case for the 2021 mega-heatwave. Also shown are upwind latent heating rates of all heatwaves from **Fig. 5a** whose air masses experienced a net potential temperature increase *en route*, again in line with the 2021 event.

Based on the limited data since 1982, the PNW stands out as the North American region most prone to experiencing a heatwave enabled by a blocking anticyclone and fueled by upwind latent heating. This hotspot set the stage for two events — in 2015, and the 2021 mega-heatwave itself — with unprecedented upwind latent heat releases compared to all other mid-latitudinal areas in the continent. In South America, the conditions for 'downwelling' summer heat are, at least based on a simple daily correlation analysis, generally less favorable than in North America or Europe, since strong relationships between 500-hPa and near-surface temperatures are largely restricted to the extratropics and mountainous terrain. While this link emerges less clearly for the highlighted region around the Pampas compared to the PNW, more events were detected for the trajectory (and hence upwind heating) analysis, and we recognize this area as an additional hotspot. There is no comparable hotspot in Australia, although we note the potential in the south and the southeast, where heatwaves are often caused by persistent anticyclones (Pezza et al., 2012; Parker et al., 2013, Quinting & Reeder, 2017). Moving on to Europe, while the British Isles feature moderate to strong upwind latent heating events, they seem unfavorable for PNW-like dynamics given that ABL heights and near-surface temperatures are generally unrelated. Geographically, and to some extent also in terms of topography, the west coast of Norway is more similar to the PNW than the British Isles, but our analysis does not reveal exceptionally strong upwind latent heating rates in this region. Therefore, the most notable hotspot in Europe is situated in-between the Black and the Caspian sea, bounded by the Caucasus mountain range to the south.

4 Conclusions

Our analysis indicates that the 2021 mega-heatwave did not occur purely by chance in the PNW, as that region has favorable conditions for strong upwind latent heating; tropical air can cross the Pacific Ocean and condense large amounts of water vapor in the process. The mountainous terrain facilitates the development of deep ABLs, and the tropospheric temperature frequently exerts control on near-surface temperature in the region. We also identified two additional hotspots — north of the Caucasus in eastern Europe, and the Pampas and surroundings in southern South America — with favorable conditions for an event with similar characteristics as in late June in the PNW. This does not, however, preclude the emergence of a heat dome elsewhere. Our findings point to the crucial role of atmospheric circulation during the 2021 PNW heatwave, which is why only simulations with constrained winds in our framework can reproduce the extreme temperature anomalies. Consequently, we cannot investigate the potential drivers behind the winds themselves such as, e.g., local and remote surface–atmosphere

interactions. Even though the role of upwind latent heating in shaping the dynamics of this event has already been recognized (Neal et al., 2022), the impact of, e.g., local and remote surface–atmosphere interactions remains unclear. This is one aspect of a bigger challenge; improving our understanding of atmospheric circulation responses to a changing climate, and the implications for extreme weather. Nevertheless, for the given winds and whether based on CESM or purely reanalysis data driven, our analyses point to a direct contribution of intense latent heating over the Pacific Ocean to downwind PNW21 heatwave temperatures of up to several degrees Celsius. This is why near-surface temperatures were even more extreme than implied by the intense anticyclonic flow, further compounded mainly by background warming and dry soils.

While existing research implies that (remote) thermodynamics in ascending humid airstreams helped shape the extreme dynamics over the PNW, this study shows that the same processes also directly exacerbated downwind heatwave temperatures. In other words, not only the (anticyclonic) circulation pattern matters, but also how it was established, owing to the origin of air and processes occurring *en route* (to the anticyclone and heatwave region) such as upwind latent heat release. We recognize that conceptualizing and compartmentalizing our Earth System and the extreme weather that it fosters has been essential to improve our understanding (e.g., Trenberth et al., 2015), yet events such as the PNW21 heatwave serve as a stark reminder of the underlying complexity. For reliable future projections, ESMs not only need to adequately represent the circulation pattern, soil moisture etc. where the extreme weather occurs, but should also accurately simulate spatiotemporal dependencies far beyond commonly considered scales, such as latent heating thousands of kilometers upwind. At last, we venture into the future and consider the implications of this event and the identified drivers. While the potential of even drier soils for the generation of more extreme heat has long been noted (e.g., Seneviratne et al., 2006a; Rasmijn et al., 2018), we highlight the possible role of stronger upwind latent heating in future hot extremes. Our atmosphere is heating up, unmistakably manifesting the consequences of an unprecedented carbon release (e.g., Mann et al., 1999; Zeebe et al., 2016; Sippel et al., 2020;). Rising air temperatures imply a non-linear increase in saturation vapor pressure, as described by the Clausius-Clapeyron relationship (Held & Soden, 2006; Hardwick Jones et al., 2010). This suggests a higher potential for heavy precipitation in the future, since air ascending from the lower to the upper troposphere — as was the case prior to the 2021 PNW heatwave and for other events — tends to rain out effectively all of its initial moisture. Therefore, in line with upward trends in extreme precipitation (e.g., Westra et al., 2013; Barbero et al., 2017), we expect that future hot events could be fueled by even more intense upwind latent heating. In fact, our research indicates that, despite eclipsing previous high temperature records in the PNW, the 2021 heatwave would have been even hotter with more moisture available over the Pacific Ocean.

Acknowledgments

The authors acknowledge funding from the European Union's Horizon 2020 research and innovation program for the "" (XAIDA) project under grant agreement 101003469. We also thank Michael Sprenger for providing most of the ERA5 data employed in the study.

Open Research

CESM version 1.2.2, the backbone of the disentangling framework employed in this study, can be downloaded from the University Corporation for Atmospheric Research (UCAR) website (https://www.cesm.ucar.edu/models/cesm1.2/). The full ERA5 dataset is accessible through ECMWF's data catalogue (https://apps.ecmwf.int/data-catalogues/era5/?class=ea). The data underlying the presented research will be uploaded to a public repository in the event of publication.

References

1. Aldama-Campino, A., Döös, K., Kjellsson, J., and Jönsson, B.: TRACMASS: Formal release of version 7.0, https://doi.org/10.5281/zenodo.4337926, 2020.
2. Ansah, E. O. & Walsh, O. S. Impact of 2021 Drought in the Pacific Northwest. *Crop. Soils* **54**, 46–49 (2021).
3. Barbero, R., Fowler, H. J., Lenderink, G. & Blenkinsop, S. Is the intensification of precipitation extremes with global warming better detected at hourly than daily resolutions? *Geophys. Res. Lett.* **44**, 974–983 (2017).
4. Barriopedro, D., Fischer, E. M., Luterbacher, J., Trigo, R. M. & García-Herrera, R. The hot summer of 2010: Redrawing the temperature record map of Europe. *Science (80-.).* **332**, 220–224 (2011).
5. Berg, A. *et al.* Impact of soil moisture-atmosphere interactions on surface temperature distribution. *J. Clim.* **27**, 7976–7993 (2014).
6. Bieli, M., Pfahl, S. & Wernli, H. A lagrangian investigation of hot and cold temperature extremes in Europe. *Q. J. R. Meteorol. Soc.* **141**, 98–108 (2015).
7. BMJ 2021;374:n1696 http://dx.doi.org/10.1136/bmj.n1696
8. Bumbaco, K.A., M.H. Rogers, L.W. O'Neill, D.J. Hoekema, C.L. Raymond. 2021 Pacific Northwest Water Year Impacts Assessment. A collaboration between the Office of the Washington State Climatologist, Climate Impacts Group, Oregon State Climatologist, Idaho Department of Water Resources, and NOAA National Integrated Drought Information System (2022).
9. Browning, K. A. Conceptual Models of Precipitation Systems. *Weather Forecast.* **1**, 23–41 (1986).
10. Center for International Earth Science Information Network (CIESIN), Columbia University. 2018. Documentation for the Gridded Population of the World, Version 4 (GPWv4), Revision 11 Data Sets. Palisades NY: NASA Socioeconomic Data and Applications Center (SEDAC). Accessed 29 April 2022, https://doi.org/10.7927/H45Q4T5F
11. Davis, C. A., Stoelinga, M. T. & Kuo, Y.-H. The Integrated Effect of Condensation in Numerical Simulations of Extratropical Cyclogenesis. *Mon. Weather Rev.* **121**, 2309–2330 (1993).
12. De Wekker, S. F. J. & Kossmann, M. Convective boundary layer heights over mountainous terrain—A review of concepts. *Front. Earth Sci.* **3**, 1–22 (2015).
13. Dey, D. & Döös, K. Atmospheric Freshwater Transport From the Atlantic to the Pacific Ocean: A Lagrangian Analysis. *Geophys. Res. Lett.* **47**, e2019GL086176 (2020).
14. Dey, D., Aldama Campino, A. & Döös, K. A complete view of the atmospheric hydrologic cycle. *Hydrol. Earth Syst. Sci. Discuss.* **25**, 1–16 (2021).
15. Döös, K.: Interocean exchange of water masses, Journal of Geophysical Research: Oceans, 100, 13 499–13 514, 1995.

16. Döös, K., Jönsson, B. & Kjellsson, J. Evaluation of oceanic and atmospheric trajectory schemes in the TRACMASS trajectory model v6.0. *Geosci. Model Dev.* **10**, 1733–1749 (2017).
17. Feudale, L. & Shukla, J. Influence of sea surface temperature on the European heat wave of 2003 summer. Part I: an observational study. *Clim. Dyn.* **36**, 1691–1703 (2011).
18. Geirinhas, J. L., Trigo, R. M., Libonati, R., Coelho, C. A. S. & Palmeira, A. C. Climatic and synoptic characterization of heat waves in Brazil. *Int. J. Climatol.* **38**, 1760–1776 (2018).
19. Hauser, M., Orth, R. & Seneviratne, S. I. Role of soil moisture versus recent climate change for the 2010 heat wave in western Russia. *Geophys. Res. Lett.* **43**, 2819–2826 (2016).
20. Hauser, M., Orth, R. & Seneviratne, S. I. Investigating soil moisture-climate interactions with prescribed soil moisture experiments: An assessment with the Community Earth System Model (version 1.2). *Geosci. Model Dev.* **10**, 1665–1677 (2017).
21. Held, I. M. & Soden, B. J. Robust responses of the hydrological cycle to global warming. *J. Clim.* **19**, 5685–5699 (2006).
22. Hersbach, H. *et al.* The ERA5 global reanalysis. *Q. J. R. Meteorol. Soc.* **146**, 1999–2049 (2020).
23. Hoskins, B. J., McIntyre, M. E. & Robertson, a. W. On the use and significance of isentropic potential vorticity maps. *Q. J. R. Meteorol. Soc.* **111**, 877–946 (1985).
24. Hurrell, J. W., Hack, J. J., Shea, D., Caron, J. M. & Rosinski, J. A new sea surface temperature and sea ice boundary dataset for the community atmosphere model. *J. Clim.* **21**, 5145–5153 (2008).
25. Hurrell, J. W. *et al.* The community earth system model: A framework for collaborative research. *Bull. Am. Meteorol. Soc.* **94**, 1339–1360 (2013).
26. Keune, J. & Miralles, D. G. A precipitation recycling network to assess freshwater vulnerability: Challenging the watershed convention. *Water Resour. Res.* **55**, 9947–9961 (2019).
27. Kornhuber, K. *et al.* Amplified Rossby waves enhance risk of concurrent heatwaves in major breadbasket regions. *Nat. Clim. Chang.* **10**, 48–53 (2020).
28. Koster, R. D. *et al.* On the nature of soil moisture in land surface models. *J. Clim.* **22**, 4322–4335 (2009).
29. Lau, N. C. & Nath, M. J. Model simulation and projection of European heat waves in present-day and future climates. *J. Clim.* **27**, 3713–3730 (2014).
30. Liang, L. & Xue, H. The Reversal Indian Ocean Waters. *Geophys. Res. Lett.* **47**, (2020).
31. Mann, M. E., Bradley, R. S. & Hughes, M. K. Northern Hemisphere temperatures during the past millennium: Inferences, uncertainties and limitations. *Geophys. Res. Lett.* **26**, 759–762 (1999).
32. Mueller, B. & Seneviratne, S. I. Hot days induced by precipitation deficits at the global scale. *Proc. Natl. Acad. Sci. U. S. A.* **109**, 12398–12403 (2012).
33. Neal, E., Huang, C. S. Y. & Nakamura, N. The 2021 Pacific Northwest heat wave and associated blocking: meteorology and the role of an upstream cyclone as a diabatic source of wave activity. *Geophys. Res. Lett.* (2022) doi:10.1029/2021gl097699.
34. Otto, F. E. L., Massey, N., Van Oldenborgh, G. J., Jones, R. G. & Allen, M. R. Reconciling two approaches to attribution of the 2010 Russian heat wave. *Geophys. Res. Lett.* **39**, 1–5 (2012).
35. Petoukhov, V. *et al.* Role of quasiresonant planetary wave dynamics in recent boreal spring-to-autumn extreme events. *Proc. Natl. Acad. Sci. U. S. A.* **113**, 6862–6867 (2016).
36. Pfahl, S., Schwierz, C., Croci-Maspoli, M., Grams, C. M. & Wernli, H. Importance of latent heat release in ascending air streams for atmospheric blocking. *Nat. Geosci.* **8**, 610–614 (2015).
37. Philip, S. Y. *et al.* Rapid attribution analysis of the extraordinary heatwave on the Pacific Coast of the US and Canada June 2021 . *World Weather Attrib.* 119–123 (2021).
38. Rasmijn, L. M. *et al.* Future equivalent of 2010 Russian heatwave intensified by weakening soil moisture constraints. *Nat. Clim. Chang.* **8**, 1–5 (2018).
39. Rey-Sanchez, C. *et al.* Evaluation of Atmospheric Boundary Layer Height From Wind Profiling Radar and Slab Models and Its Responses to Seasonality of Land Cover, Subsidence, and Advection. *J. Geophys. Res. Atmos.* **126**, 1–32 (2021).

40. Robine, J. M. *et al.* Death toll exceeded 70,000 in Europe during the summer of 2003. *C. R. Biol.* **331**, 171–178 (2008).
41. Rex, D. F. Blocking Action in the Middle Troposphere and its Effect upon Regional Climate. *Tellus* **2**, 275–301 (1950).
42. Rossby, C.-G. Relation between variations in the intensity of the zonal circulation of the atmosphere and the displacements of the semi-permanent centers of action. *J. Mar. Res.* **2**, 38–55 (1939).
43. Röthlisberger, M., Pfahl, S. & Martius, O. Regional-scale jet waviness modulates the occurrence of midlatitude weather extremes. *Geophys. Res. Lett.* **43**, 10,989-10,997 (2016).
44. Sánchez-Benítez, A., García-Herrera, R., Barriopedro, D., Sousa, P. M. & Trigo, R. M. June 2017: The earliest European summer mega-heatwave of reanalysis period. *Geophys. Res. Lett.* **45**, 1955–1962 (2018).
45. Samenow, J. and Livingston, I., June 29, 2021. Canada sets new all-time heat record of 121 degrees amid unprecedented heat wave. *The Washington Post.* https://www.washingtonpost.com/weather/2021/06/27/heat-records-pacific-northwest/
46. Schäfler, A. & Harnisch, F. Impact of the inflow moisture on the evolution of a warm conveyor belt. *Q. J. R. Meteorol. Soc.* **141**, 299–310 (2015).
47. Schumacher, D. L. *et al.* Amplification of mega-heatwaves through heat torrents fuelled by upwind drought. *Nat. Geosci.* **12**, 712–717 (2019).
48. Seneviratne, S. I., Lüthi, D., Litschi, M. & Schär, C. Land-atmosphere coupling and climate change in Europe. *Nature* **443**, 205–209 (2006a).
49. Seneviratne, S. I. *et al.* Soil moisture memory in AGCM simulations: Analysis of global land-atmosphere coupling experiment (GLACE) data. *J. Hydrometeorol.* **7**, 1090–1112 (2006b).
50. Seneviratne, S.I., T. Corti, E.L. Davin, M. Hirschi, E.B. Jaeger, I. Lehner, B. Orlowsky, and A.J. Teuling, 2010: Investigating soil moisture-climate interactions in a changing climate: A review. Earth-Science Reviews, 99, 3-4, 125-161, doi:10.1016/j.earscirev.2010.02.004.
51. Seneviratne, S.I., M. Wilhelm, T. Stanelle, B.J.J.M. van den Hurk, S. Hagemann, A. Berg, F. Cheruy, M.E. Higgins, A. Meier, V. Brovkin, M. Claussen, A. Ducharne, J.-L. Dufresne, K.L. Findell, J. Ghattas, D.M. Lawrence, S. Malyshev, M. Rummukainen, and B. Smith, 2013: Impact of soil moisture-climate feedbacks on CMIP5 projections: First results from the GLACE-CMIP5 experiment. Geophys. Res. Lett., 40 (19), 5212-5217
52. Sherwood, S. C., Roca, R., Weckwerth, T. M. & Andronova, N. G. Tropospheric water vapor, convection, and climate. *Rev. Geophys.* **48**, 1–29 (2010).
53. Sippel, S., Meinshausen, N., Fischer, E. M., Székely, E. & Knutti, R. Climate change now detectable from any single day of weather at global scale. *Nat. Clim. Chang.* **10**, 35–41 (2020).
54. Sodemann, H., Schwierz, C. & Wernli, H. Interannual variability of Greenland winter precipitation sources: Lagrangian moisture diagnostic and North Atlantic Oscillation influence. *J. Geophys. Res.* **113**, 1–17 (2008).
55. Sousa, P. M., Trigo, R. M., Barriopedro, D., Soares, P. M. M. & Santos, J. A. European temperature responses to blocking and ridge regional patterns. *Clim. Dyn.* **50**, 457–477 (2018).
56. Stéfanon, M., Drobinski, P., D'Andrea, F., Lebeaupin-Brossier, C. & Bastin, S. Soil moisture-temperature feedbacks at meso-scale during summer heat waves over Western Europe. *Clim. Dyn.* **42**, 1309–1324 (2014).
57. Steinfeld, D. & Pfahl, S. The role of latent heating in atmospheric blocking dynamics: a global climatology. *Clim. Dyn.* **53**, 6159–6180 (2019).
58. Steinfeld, D., Boettcher, M., Forbes, R. & Pfahl, S. The sensitivity of atmospheric blocking to upstream latent heating – numerical experiments. *Weather Clim. Dyn.* **1**, 405–426 (2020).
59. Stohl, A. & Seibert, P. Accuracy of trajectories as determined from the conservation of meteorological tracers. *Q. J. R. Meteorol. Soc.* **124**, 1465–1484 (1998).
60. Stoelinga, M. T. A potential vorticity-based study of the role of diabatic heating and friction in a numerically simulated baroclinic cyclone. *Mon. Weather Rev.* **124**, 849–874 (1996).

61. Stott, P. A., Stone, D. A. & Allen, M. R. Human contribution to the European heatwave of 2003. *Nature* **432**, 610–614 (2004).
62. Stott, P. A. *et al.* Attribution of extreme weather and climate-related events. *Wiley Interdiscip. Rev. Clim. Chang.* **7**, 23–41 (2016).
63. Thompson, V. *et al.* The 2021 western North America heat wave among the most extreme events ever recorded globally. 1–11 (2022).
64. Trenberth, K. E., Fasullo, J. T. & Shepherd, T. G. Attribution of climate extreme events. *Nat. Clim. Chang.* **5**, 725–730 (2015).
65. Trigo, R. M., García-Herrera, R., Díaz, J., Trigo, I. F. & Valente, M. A. How exceptional was the early August 2003 heatwave in France? *Geophys. Res. Lett.* **32**, 1–4 (2005).
66. Troen, I. B. & Mahrt, L. A simple model of the atmospheric boundary layer; sensitivity to surface evaporation. *Boundary-Layer Meteorol.* **37**, 129–148 (1986).
67. van Oldenborgh, G. J. *et al.* Pathways and pitfalls in extreme event attribution. *Clim. Change* **166**, 1–27 (2021).
68. Wang, H., Schubert, S., Koster, R., Ham, Y. G. & Suarez, M. On the role of SST forcing in the 2011 and 2012 extreme U.S. heat and drought: A study in contrasts. *J. Hydrometeorol.* **15**, 1255–1273 (2014).
69. Wehrli, K., Guillod, B. P., Hauser, M., Leclair, M. & Seneviratne, S. I. Assessing the dynamic versus thermodynamic origin of climate model biases. *Geophys. Res. Lett.* **45**, 8471–8479 (2018).
70. Wehrli, K., Guillod, B. P., Hauser, M., Leclair, M. & Seneviratne, S. I. Identifying key driving processes of major recent heatwaves. *J. Geophys. Res. Atmos.* **124**, 11746–11765 (2019).
71. Wehrli, K., Hauser, M. & Seneviratne, S. I. Storylines of the 2018 Northern Hemisphere heatwave at pre-industrial and higher global warming levels. *Earth Syst. Dyn.* **11**, 855–873 (2020).
72. Wehrli, K. *et al.* The ExtremeX global climate model experiment : Investigating thermodynamic and dynamic processes contributing to weather and climate extremes. *Earth Syst. Dyn. Discuss.* 1–31 (2021).
73. Westra, S., Alexander, L. V. & Zwiers, F. W. Global increasing trends in annual maximum daily precipitation. *J. Clim.* **26**, 3904–3918 (2013).
74. Yao, Y., Luo, D., Dai, A. & Simmonds, I. Increased quasi stationarity and persistence of winter ural blocking and Eurasian extreme cold events in response to arctic warming. Part I: Insights from observational analyses. *J. Clim.* **30**, 3549–3568 (2017).
75. Zampieri, M. *et al.* Hot European summers and the role of soil moisture in the propagation of mediterranean drought. *J. Clim.* **22**, 4747–4758 (2009).
76. Zaitchik, B. F., Macalady, A. K., Bonneau, L. R. & Smith, R. B. Europe's 2003 heat wave: A satellite view of impacts and land - Atmosphere feedbacks. *Int. J. Climatol.* **26**, 743–769 (2006).
77. Zeebe, R. E., Ridgwell, A. & Zachos, J. C. Anthropogenic carbon release rate unprecedented during the past 66 million years. *Nat. Geosci.* **9**, 325–329 (2016).
78. Zschenderlein, P., Pfahl, S., Wernli, H. & Fink, A. H. A Lagrangian analysis of upper-tropospheric anticyclones associated with heat waves in Europe. *Weather Clim. Dyn.* **1**, 191–206 (2020).
79. Vogel, M.M., J. Zscheischler, and S.I. Seneviratne, 2018: Varying soil moisture-atmosphere feedbacks explain divergent temperature extremes and precipitation in central Europe. Earth System Dynamics, 9, 1107-1125.